

## RESEARCH ARTICLE

# A spiral planar inductor: An experimentally verified physically based model for frequency and time domains

Aymen Ammouri<sup>1</sup> | Tarek Ben Salah<sup>1</sup>  | Herve Morel<sup>2</sup> 

<sup>1</sup> ENIT-L.S.E, University of Tunis El Manar, BP 37-1002 Tunis, Tunisia

<sup>2</sup> Université of Lyon, INSA-Lyon, Lab. Ampere, CNRS, Villeurbanne, Lyon, France

## Correspondence

Tarek Ben Salah, ENIT-L.S.E, University of Tunis El Manar, BP 37-1002, Tunis, Tunisia.  
Email: tarek.bensalah@gmail.com

## Abstract

The results of a comprehensive investigation of spiral inductors are presented. A physically based model includes the self and mutual inductances, the capacitances between adjacent turns, the substrate capacitance, and the ohmic loss effects proposed. Heterogeneous simulation scheme, including circuit and device models during time and frequency domains, is successfully implemented in VHDL-AMS language and is simulated numerically in Simplorer platform. The model has been validated during frequency domain with measurement data of spirals having different geometries and various sizes. Moreover, the fabricated spiral inductors are evaluated in DC-DC power converter to benchmark the model accuracy. Simulation and experimental results show excellent agreement. Validity domain is discussed.

## KEYWORDS

experiment, inductor model, spiral planar inductor

## 1 | INTRODUCTION

In the work of Ouyang and Andersen,<sup>1</sup> they specified various problems related to the integration of power electronic systems. The authors demonstrated that the large mass/volume of a given power system is occupied by magnetic components. These components may be optimized using planar printed circuit board (PCB) devices. Compared with the conventional magnetic components, planar technology is printed directly on circuit board (PCB) with low profile and offers the flexibility of winding geometry and large shape.<sup>1-3</sup>

From a design point of view, planar inductor electrical behavior cannot be precisely predicted by the conventional inductor models.<sup>4-6</sup> In particular, the skin, the proximity, and the parasitic capacitances effects are complex devices to model, particularly during large frequency domain. In the work of Han et al.,<sup>5</sup> the electromagnetic simulation is considered to be modeling planar components. However, this method is not only cumbersome and time-consuming but also difficult to develop into general electronically circuit simulations. Other original models are reported by Wang et al.<sup>6</sup> However, this model is not dependent on the geometrical parameters and the layout process. Moreover, its model parameters are not used fairly to optimize the planar inductor layout. In a previous work,<sup>3</sup> a simple square planar inductor model is developed and simulated inside a power converter during time domain.<sup>7</sup> However, the validation process appeared quite limited at frequency domain and for different planar inductor structures such as hexagonal and octagonal structures (Figure 1). So far, literature has addressed models of planar inductor but was not able to simulate different inductor designs. It is thus necessary to assess the planar inductor electrical performances and its validation not only during time domain but also during frequency domain for different inductor structures.

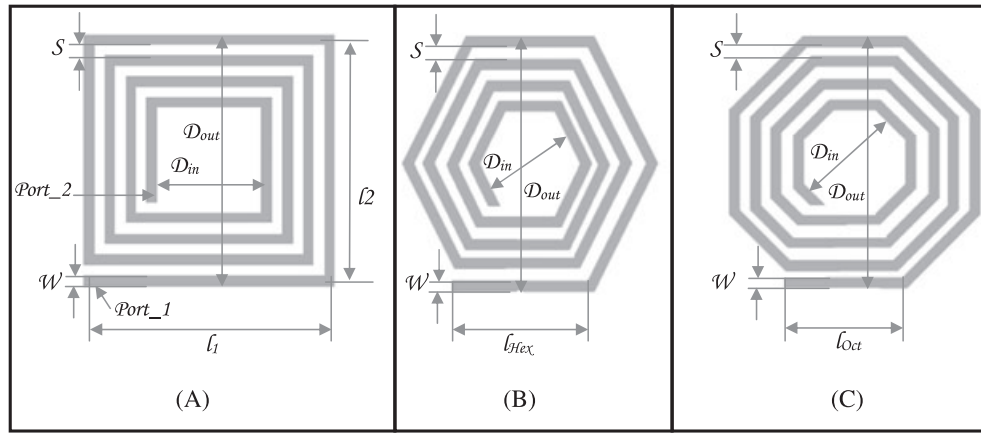


**FIGURE 1** Inductor geometries: A, square; B, hexagonal; C, octagonal

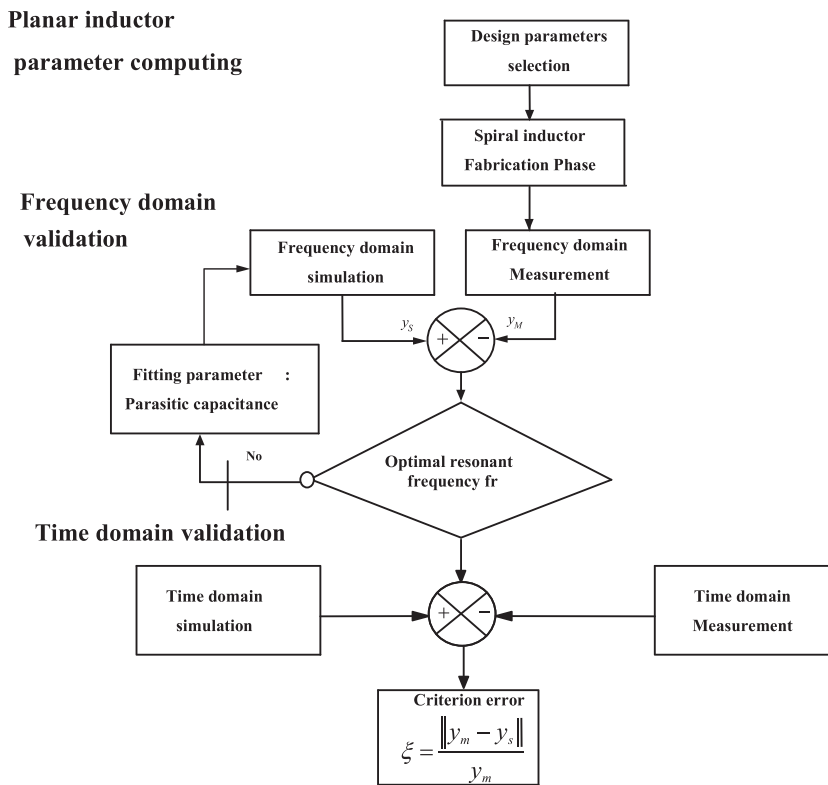


**FIGURE 2** The procedure used during time and frequency domain validations

The principal purpose of this paper is to present an accurate physically based planar inductor model able to simulate different inductor structures such as square, hexagonal, and octagonal structures.

During validation process, a flowchart algorithm is proposed (Figure 2).

- First, the planar inductors parameters are selected: The layout of square, hexagonal, and octagonal planar inductors is considered, and the design parameters are computed.
- Second, we compare the simulated results with the experimental measurements at frequency domain for several shape designs.
- Finally, the planar inductor model is revalidated during time domain. The device simulation results are confronted with experimental data for several inductor designs.

The errors between experimental and simulation waveforms are computed to estimate the validation quality.

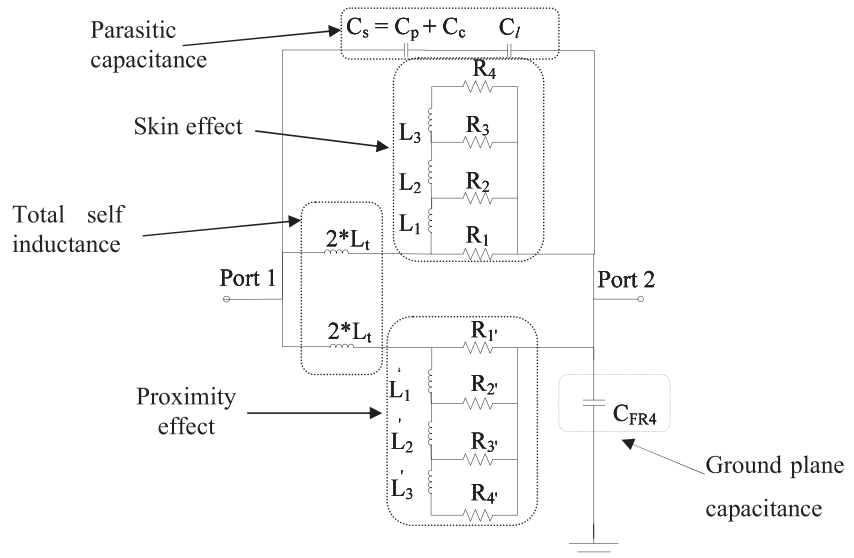


**FIGURE 3** Equivalent-circuit model of a planar inductor

## 2 | PLANAR INDUCTOR MODEL

Figure 3 presents the proposed planar inductor equivalent-circuit model, where  $L_t$  represents the DC total inductance including the self and mutual inductances. The skin and proximity effects in metal trace are modeled by an  $RL$  ladder structure.<sup>7</sup> The  $RL$  circuit is mainly dependent on the current crowding in the metal. The capacitance  $C_s$ —the parasitic capacitance—is the sum of interline capacitances between the spirals,  $C_p$ , and the capacitance between the spirals and the underpass,  $C_c$ . The capacitance  $C_l$ —the parasitic effect due to the electric loss of the substrate—is also integrated to modeling the decrease of effective resistance.<sup>8</sup> Finally,  $C_{FR4}$  represents the ground plane bulk capacitance model. Complete details of the proposed model equations are summarized in Tables 1–4.

### 2.1 | Total inductance model

Equations 1 and 2 (Table 1) give the model of the total length for square, hexagonal, and octagonal planar inductor estimated as follows: For a square spiral inductor (Figure 1A), total length is calculated by an index  $i$ , which corresponds to the subscript number of the wire segment in the planar inductor, with  $i \geq 2$ . In this case, the lengths  $l_1$  and  $l_2$  are equal to the planar inductor external diameter. The regular hexagonal and octagonal inductor designs (Figure 1B,C) are computed with a polygon with 6 and 8 equal sides, respectively. The lengths of the wire segment in the hexagonal and octagonal planar inductors,  $l_{Hex\_i}$  and  $l_{Oct\_i}$ , are determined by expressions 4 and 5, respectively.

The total inductance of the planar inductor  $L_t$  is given by Equation 6. Equation 6 is computed by summing the self-inductance of each wire segment  $L_s$  and the positive and negative mutual inductances ( $M_p$  and  $M_n$ ) between any parallel segments. The self-inductance of a rectangular cross-sectional area wire segment is also calculated by Equation 7.<sup>9,10</sup> The total self-inductance of an  $n$ -turn polygonal spiral is expressed by Equation 8. The parameter  $\alpha$  included in Equation 8 represents the number of sides for one turn in polygonal planar inductor, where  $\alpha$  is equal to 4, 6, and 8 for square, hexagonal, and octagonal inductances correspondingly, for instance.

The positive mutual inductance is the sum of mutual inductances between parallel lines when the direction of their currents is the same.<sup>11</sup> The negative mutual inductance is also the sum of mutual inductances between parallel lines, in the case of currents in opposite direction. Compact and simple expressions for the positive and negative mutual inductances of a square planar inductor are given by Equations 9 and 11, respectively (Table 1). The computing of the hexagonal and octagonal inductor models is extracted from the square planar inductor model. Our contribution consists of extrapolating the hexagonal and octagonal models from a square model equation as detailed in Table 2.

### 2.2 | Resistance model of planar inductor

The resistance of the inductance origin is from the metal resistivity. Therefore, at DC mode, the current density is uniform. In this case, the resistance  $R_{dc}$  of a wire with a rectangular cross section is given by expression 17.<sup>7</sup> It is worth noting that, at

**TABLE 1** Planar inductance model

Expression	Equation Number	Model
$l_{2i-1}$	(1)	$l_1 - (i-2)(\omega + s)$ , where $i \geq 2$
$l_{2i}$	(2)	$l_2 - (i-1)(\omega + s)$ , where $i \geq 2$
$l_{i+1}$	(3)	$l_1 - (i^*m)$ , where $i = 0 : 1 : n-1$
		$m = 2^* \sqrt{\left(\frac{(\omega+s)}{(\sin(60))}\right)^2 - (\omega+s)^2}$ hexagonal inductor
		$m = 2^* \sqrt{\left(\frac{(\omega+s)}{(\sin(67.5))}\right)^2 - (\omega+s)^2}$ octagonal inductor
$l_{\text{Hex}_i}$	(4)	$D_{\text{out}_i} / \sqrt{3}$
$l_{\text{Oct}_i}$	(5)	$D_{\text{out}_i} / 1 + 2 \cos(\frac{\pi}{4})$
$L_t$	(6)	$L_s + M_p - M_n$
$L_{\text{self}}$	(7)	$\frac{\mu_0}{2\pi} l \left[ \ln\left(\frac{2l}{\omega+t}\right) + 0.5 + \left(\frac{\omega+t}{3l}\right) \right]$
$L_s$	(8)	$\sum_{i=1}^{\alpha^* n} L_i = \sum_{i=1}^{\alpha^* n} \frac{\mu_0}{2\pi} l_i \left[ \ln\left(\frac{2l_i}{\omega+t}\right) + 0.5 + \left(\frac{\omega+t}{3l_i}\right) \right]$
$M^+$	(9)	$\frac{\mu_0}{2\pi} l_{\text{sq}} (n-1) \left[ \ln\left(\sqrt{1 + \left(\frac{l_{\text{sq}}}{4nd^+}\right)^2} + \frac{l_{\text{sq}}}{4nd^+}\right) - \sqrt{1 + \left(\frac{4nd^+}{l_{\text{sq}}}\right)^2} + \frac{4nd^+}{l_{\text{sq}}}\right]$
$d^+$	(10)	$(\omega + s) \frac{(3n-2N_i-1)(N_i+1)}{3(2n-N_i-1)}$
$M^-$	(11)	$0.47 \frac{\mu_0}{2\pi} * l_{\text{sq}}^* n$

$\mu_0$  is the permeability of vacuum,  $d^+$  is the average distance between all segments used to compute the positive mutual inductance,  $N_i$  is the integer part of the number of turns  $n$ , and  $l_{\text{sq}}$  is the total length of the square planar inductor.

high frequency, the current distribution in the metallic line becomes nonuniform, which is caused by the skin and proximity effects.

In the case of a circular cross-sectional design, the metal line with a circular cross section is divided into 4 concentric regions: 4 resistances from  $R_1$  to  $R_4$  and 3 inductors from  $L_1$  to  $L_3$ . Therefore, the skin effect is outlined by a ladder circuit. The proximity effect is constructed by further extending ( $RL$  ladder structure) as shown in Figure 3. The resistance  $R_1$  is computed by expression 18, and the skin depth in the meal line is calculated at the maximum simulation frequency (Equation 19). Finally, the resistance and the inductance of the ladder structure are resolved by Equations 20 and 21, respectively (Table 3).

The resistance and inductance ratio parameters  $\Gamma_R$  and  $\Gamma_L$  included in Equations 20 and 21 are generally constant. These 2 parameters are given by the cubic Equation 18 and the polynomial Equation 26. The parameters  $\alpha_R$  and  $\alpha_L$  are established by Equations 23 and 27, correspondingly. It is worth noting that the ladder circuit parameter,  $L_1$ , is related to the internal inductance  $L_{\text{int}}$  of a planar inductor as expressed by Equation 24. Therefore, the internal inductance  $L_{\text{int}}$ , associated with the metallic trace with rectangular cross section at low frequencies, is given by Equation 25.<sup>12</sup>

The proximity effect model, which presents the evolution of the resistance versus frequency, is modeled by an extending  $RL$  ladder circuit. The ladder circuit of proximity effect is connected in parallel with the circuit of the skin effect as shown in Figure 3. The  $RL$  ladder circuits of skin and proximity effects are divided by  $(\xi)$  and  $(1-\xi)$ , respectively, where  $\xi$  represents the width ratio calculated by Equation 28. When the total mutual inductance is very small, the proximity effect became low, and thus  $\xi$  equals to 0.5.

## 2.3 | Capacitance models of planar inductor

The capacitance between adjacent turns is considered by decomposing the effect into 2 types of insulating materials. The first insulator is the air that fills the gap between adjacent traces. The second one is the substrate of a planar inductor, which is FR4 in our study. The parasitic capacitance is detailed in Equation 29 (see Table 4). The 2 factors,  $\alpha$  and  $\beta$ , included in Equation 29 associated with the air and the FR4 insulators are empirically tuned. In our case,  $\alpha$  and  $\beta$  are equal to 0.9 and 0.1, respectively.<sup>13</sup> The coupling capacitance between the spiral and underpass is shown by the sum of all overlap capacitances (Equation 30). The

**TABLE 2** Square, hexagonal, and octagonal planar inductance models

Expression	Equation Number	Model
$L_{\text{t\_Square}}$	(12)	$\frac{\mu_0}{2\pi} \left[ \begin{aligned} &\sum_{i=1}^{4^*n} l_{sqi} \left[ \ln \left( \frac{2l_{sqi}}{\omega + t} \right) + 0.5 + \left( \frac{\omega + t}{3l_{sqi}} \right) \right] \\ &+ l_{sq}(n-1) \left[ \begin{aligned} &\ln \left( \sqrt{1 + \left( l_{sq} / 4nd^+ \right)^2} + \frac{l_{sq}}{4nd^+} \right) \\ &\sqrt{1 + \left( 4nd^+ / l_{sq} \right)^2} + \frac{4nd^+}{l_{sq}} \end{aligned} \right] \\ &+ 0.47^* l_{sq}^* n \end{aligned} \right]$
$L_{\text{t\_Hexagonal}}$	(13)	$\frac{\mu_0}{2\pi} \left[ \begin{aligned} &\sum_{i=1}^{6^*n} l_{\text{Hex}i} \left[ \ln \left( \frac{2l_{\text{Hex}i}}{\omega + t} \right) + 0.5 + \left( \frac{\omega + t}{3l_{\text{Hex}i}} \right) \right] \\ &+ l_{\text{Hex}}(n-1) \left[ \begin{aligned} &\ln \left( \sqrt{1 + \left( l_{\text{Hex}} / 4nd^+ \right)^2} + \frac{l_{\text{Hex}}}{4nd^+} \right) \\ &\sqrt{1 + \left( 4nd^+ / l_{\text{Hex}} \right)^2} + \frac{4nd^+}{l_{\text{Hex}}} \end{aligned} \right] \\ &+ 0.47^* l_{\text{Hex}}^* n \end{aligned} \right]$
$L_{\text{t\_Octagonal}}$	(14)	$\frac{\mu_0}{2\pi} \left[ \begin{aligned} &\sum_{i=1}^{8^*n} l_{\text{Oct}i} \left[ \ln \left( \frac{2l_{\text{Oct}i}}{\omega + t} \right) + 0.5 + \left( \frac{\omega + t}{3l_{\text{Oct}i}} \right) \right] \\ &+ l_{\text{Oct}}(n-1) \left[ \begin{aligned} &\ln \left( \sqrt{1 + \left( l_{\text{Oct}} / 4nd^+ \right)^2} + \frac{l_{\text{Oct}}}{4nd^+} \right) \\ &\sqrt{1 + \left( 4nd^+ / l_{\text{Oct}} \right)^2} + \frac{4nd^+}{l_{\text{Oct}}} \end{aligned} \right] \\ &+ 0.47^* l_{\text{Oct}}^* n \end{aligned} \right]$
$l_{\text{Hex}}$	(15)	$\frac{l_{sq}}{1.33}$ with $l_{sq} = 4n \left( \frac{l_{\text{Hex}}}{6n} + 2 \frac{l_{\text{Hex}}}{6n} \cos 60^\circ \right)$
$l_{\text{Oct}}$	(16)	$\frac{l_{sq}}{1.21}$ with $l_{sq} = 4n \left( \frac{l_{\text{Oct}}}{8n} + 2 \frac{l_{\text{Oct}}}{8n} \cos 45^\circ \right)$

$l_{sq_i}$ ,  $l_{\text{Hex}_i}$ , and  $l_{\text{Oct}_i}$  represent respectively the length of the wire segment in the square, hexagonal, and octagonal planar inductors.  $l_{sq}$ ,  $l_{\text{Hex}}$ , and  $l_{\text{Oct}}$  represent respectively the total length of the square, hexagonal, and octagonal planar inductors.

**TABLE 3** Planar inductor model: resistance expressions

Expression	Equation Number	Form
$R_{\text{dc}}$	(17)	$\rho \frac{l}{wt}$
$R_1$	(18)	$\frac{l}{2t\sigma\delta_{\text{max}}}$
$\delta_{\text{max}}$	(19)	$\sqrt{\frac{1}{\pi\mu\sigma f_{\text{max}}}}$
$\Gamma_{\text{R}}$	(20)	$\frac{R_{i+1}}{R_i} \quad i = 1, 2, 3$
$\Gamma_{\text{L}}$	(21)	$\frac{L_i}{L_{i+1}} \quad i = 1, 2$
	(22)	$\Gamma_{\text{R}}^3 + \Gamma_{\text{R}}^2 + \Gamma_{\text{R}} + (1 - \alpha_{\text{R}}) = 0$
$\alpha_{\text{R}}$	(23)	$\frac{R_1}{R_{\text{dc}}}$
$L_1$	(24)	$\frac{L_{\text{int}}}{\alpha_{\text{L}}}$
$L_{\text{int}}$	(25)	$l^* (0.3 + 0.28^* \exp(-0.14 \frac{\omega}{l}))$
	(26)	$\Gamma_{\text{L}}^{-2} + (1 + \Gamma_{\text{R}}^{-1})^2 \Gamma_{\text{L}}^{-1} + (1 + \Gamma_{\text{R}}^{-1} + \Gamma_{\text{R}}^{-2})^2 - \alpha_{\text{L}}((1 + \Gamma_{\text{R}}^{-1})(1 + \Gamma_{\text{R}}^{-2}))^2 = 0$
$\alpha_{\text{L}}$	(27)	$0.2^* \alpha_{\text{R}}$
$\xi$	(28)	$\sqrt{\frac{\left(\frac{L_{\text{S}}}{2M_i}\right)^2 + 1 - \left(\frac{L_{\text{S}}}{2M_i}\right) + 1}{2}}$

$\rho$  is the resistivity of the metal,  $\sigma$  is the conductivity of the metal trace,  $l$  is the length of the planar inductor,  $\delta_{\text{max}}$  is the skin depth at the maximum simulation frequency, and  $f_{\text{max}}$  is the highest simulation frequency.

**TABLE 4** Model capacitances of the planar inductor

Expression	Equation Number	Model
$C_p$	(29)	$C_{pc} + C_{ps} \approx \epsilon_0 \frac{T}{S} l_t (\alpha \epsilon_{rc} + \beta \epsilon_{rs})$
$C_c$	(30)	$n w^2 \frac{\epsilon_{ox}}{t_{oxM1-M2}}$
$f_r$	(31)	$\frac{1}{2\pi \sqrt{L_0 C_1}}$

$\epsilon_0$ ,  $\epsilon_{rc}$ , and  $\epsilon_{rs}$  are the permittivity of vacuum and the relative dielectric constants of the coating and substrate materials, respectively, with  $(\epsilon_{rc}; \epsilon_{rs}) = (1; 4.4)$  from insulator,  $n$  is the number of overlap,  $\epsilon_{ox}$  is the dielectric constant, and  $t_{oxM1-M2}$  is the oxide thickness between the spiral and the underpass.  $L_0$  is the inductance value at low frequency, and  $C_1$  is the total capacitance value.

self-resonant role is to resolve the limit of operation frequency in the inductor. Therefore, the self-resonant frequency  $f_r$ , due to parasitic capacitances at high frequencies, is identified when the reactance of the planar inductor is zero.<sup>14</sup>

The capacitance  $C_1$  represents the isolation capacitance between the input and output terminals. The substrate coupling capacitance  $C_1$  can be attributed to the resonance in the planar inductor and in the work of Jow and Ghovanloo.<sup>13</sup> Therefore, using the resonance frequency, the capacitance  $C_1$  can be extracted from expression 31.

### 3 | VALIDATION PROCESS

#### 3.1 | Planar inductor parameter computing

Before fabrication process, the finest and high-quality planar inductor factors are studied by analyzing the optimal number of turns of a given device.<sup>15,16</sup> In particular, Su et al<sup>15</sup> demonstrate that the optimal planar inductor hollow factor—defined by the ratio between the inner and outer radii of winding—achieves a maximal quality factor and a high inductance value. Su et al<sup>15</sup> reveal that the high-quality factor is obtained for a factor  $\Gamma$  between 0.45 and 0.55. On the other hand, the current in the ground plane reduces the total magnetic flux induced by the inductor and consequentially reduces the value of the inductance.<sup>16</sup> Absolutely, there is a trade-off between the ground plane geometries and the  $\Gamma$  factor. On the basis of this background, optimal design parameters of the square, hexagonal, and octagonal planar inductors are selected as shown in Table 5. The optimization process is not taken into account. The latter choices are adequate for compact spiral inductor design. They are not discussed here as these issues are beyond the scope of the paper.

The model parameters of 3 inductors are considered from experimental and simulation points of view. Therefore, the outer diameter and the thickness of metal trace are set to 40 mm and 0.35  $\mu\text{m}$ , respectively. The width of the inductor PCB layout is set from 0.8 to 0.6 mm, and the spacing between turns is increased from 0.4 to 0.6 mm. The number of turns is also selected to have a better fill factor ( $\Gamma$ ) and a maximum quality factor with high inductance value. Figure 4 shows some spiral planar inductor sample fabricated using FR4 PCB as a substrate with a dielectric constant,  $\epsilon_r$ , and PCB substrate thickness (4.4 and 1.6 mm). These devices are used here during and after time and frequency domain validation processes.

**TABLE 5** Optimal design parameters used during experimental process

Design Parameters	Square 1 Hexagonal 1 Octagonal 1	Square 2 Hexagonal 2 Octagonal 2	Square 3 Hexagonal 3 Octagonal 3
$D_{out}$ , mm	40	40	40
$D_{in}$ , mm	16.8	21.6	18.8
$\Gamma = \frac{D_{in}}{D_{out}}$	0.42	0.54	0.47
W, mm	0.6	0.8	0.8
S, mm	0.4	0.4	0.6
$t$ , $\mu\text{m}$	35	35	35
N	12	8	8

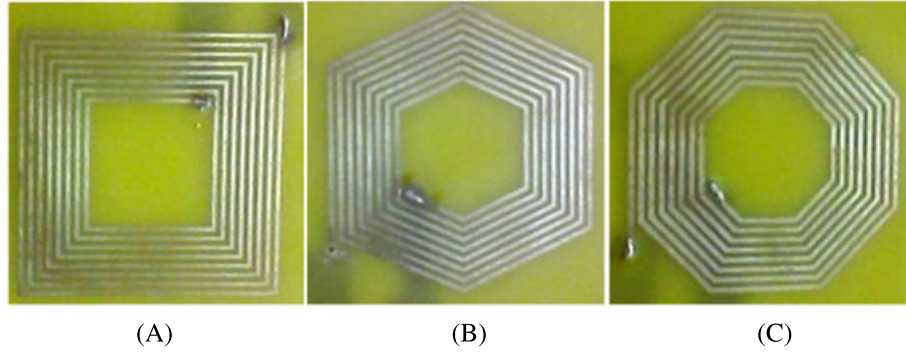


**FIGURE 4** Tested printed circuit board planar spiral inductors: A, square; B, hexagonal; C, octagonal

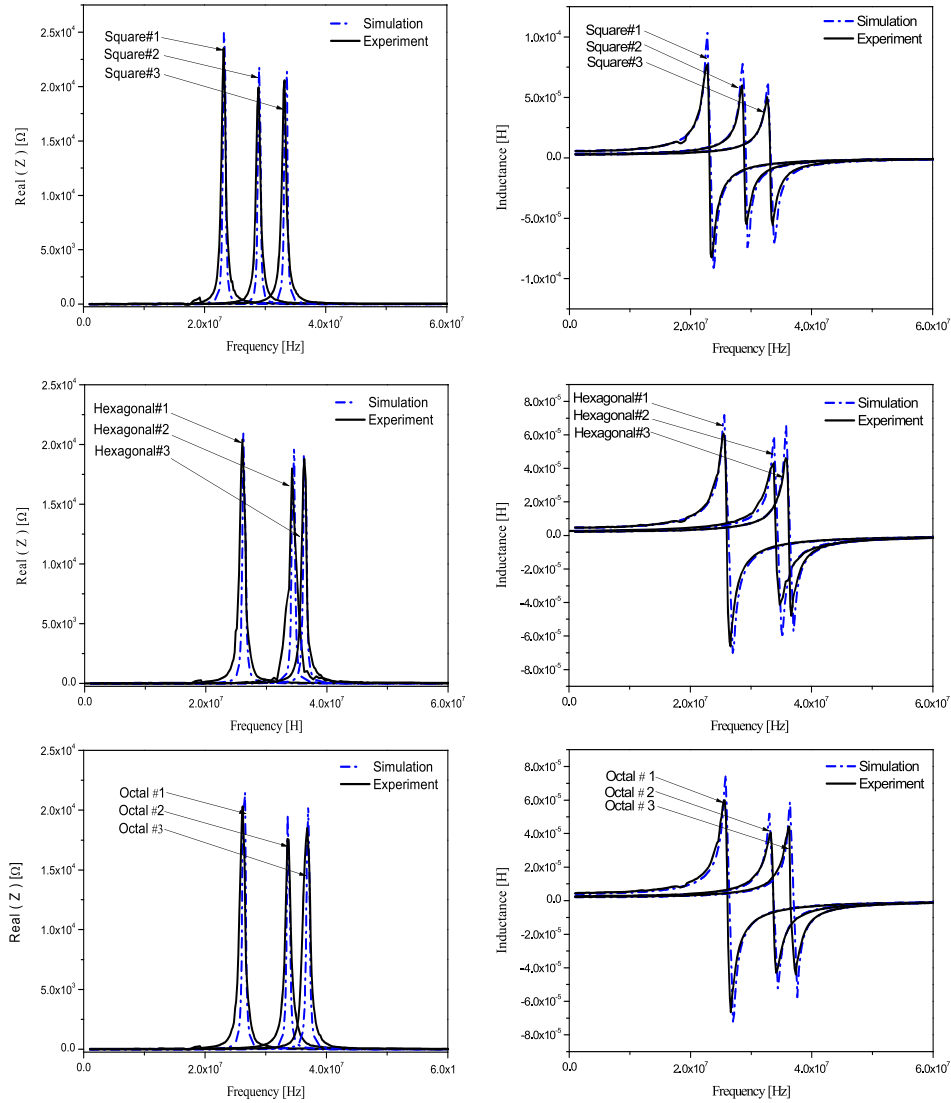


**FIGURE 5** A comparative study between experimental data and simulation results of electrical characteristic versus frequency for different planar inductors: A, square; B, hexagonal; C, octagonal

### 3.2 | Frequency domain validation

During frequency domain analysis, the planar inductors are characterized by the vector network analyzer. The range of frequencies is from 1 to 100 MHz. For frequencies above self-resonant frequency, the effects of the equivalent capacitance of inductor



become significant. With just 1 port, ie, 2 connection points, both ends of the spiral inductor are measured between the signal connected to Port-1 (phase) and port-2 (neutral) which is referring to ground.

The frequency domain validation is based on the optimization error between experimental and simulation. Figure 5 depicts a comparative study between experimental and simulation results of different planar inductor designs. Figure 5 demonstrates that the proposed equivalent-circuit model can be deemed suitable to represent the planar inductor useful for system-level circuit simulation during frequency domain. Indeed, a tiny error between simulation and experimental waveforms is observed at low frequencies. It is the authors' opinion that this error is mainly due to the parasitic effect probes connections.<sup>17</sup> Otherwise, the additional probes model complexity during frequency domain simulation is not worth the small incremental accuracy.

At high frequencies, the skin and proximity effects dominate, and the resistance of the inductor increases versus the frequency. Thereby, the appearance of the capacitive effect is due to the interturn capacity. The resonant frequency marks the point where the inductor becomes capacitance, and thus, when the parasitic capacitances are larger, the resonant frequency is lower.<sup>14</sup> Table 6 summarizes the error between experimental results and simulation data for the electrical parameters ( $L_s$ ,  $R_s$ ) of the square, hexagonal, and octagonal spiral inductor designs. The value of inductance  $L_s$  (the imaginary part of the complex impedance) is determined at 1 MHz, and the real part of the complex impedance resistance  $Z_{re}$  is extracted from the resonant frequency. The error denoted as  $\delta$  is calculated according to the following expression<sup>12</sup>:

$$\delta = \left| \frac{f_{\text{mea}}(x_i) - f_{\text{sim}}(x_i)}{f_{\text{mea}}(x_i)} \right| \quad (32)$$

where  $f_{\text{mea}}$  and  $f_{\text{sim}}$  are the electrical quantities extracted from the measured data and simulated result, respectively.

**TABLE 6** Errors between simulation and experiment of different planar inductors during frequency domain validation

Inductor/Parameter		$L_s$ , $\mu\text{H}$	$Z_{re}$ , $\Omega$
Square 1	Simulation	5.71	24 935
	Experimental	5.54	23 520
	Error %	3	6
Hexagonal 1	Simulation	4.69	21 003
	Experimental	4.61	20 400
	Error %	1.7	2.9
Octagonal 1	Simulation	4.42	21 502
	Experimental	4.26	20 298
	Error %	3.7	5.9
Square 2	Simulation	3.28	21 770
	Experimental	3.07	19 925
	Error %	6.8	9.2
Hexagonal 2	Simulation	2.72	19 843
	Experimental	2.71	17 992
	Error %	0.3	10.2
Octagonal 2	Simulation	2.47	19 120
	Experimental	2.59	17 590
	Error %	4.6	8.6
Square 3	Simulation	2.85	21 352
	Experimental	2.69	20 573
	Error %	5.9	3.7
Hexagonal 3	Simulation	2.36	19 155
	Experimental	2.29	18 782
	Error %	3	1.9
Octagonal 3	Simulation	2.21	20 382
	Experimental	2.13	18 484
	Error %	3.7	10.2



### 3.3 | Time domain validation

Figure 6 shows the proposed experimental test bench circuit. During this step, different planar inductor designs are integrated in a simple power converter. The spiral inductor role is the circuit inductance load,  $L$ , which defines the switching turn-off parameters  $dv/dt$  and  $di/dt$  of the transistor.<sup>3,18</sup> The experimental platform integrates also the following elements:

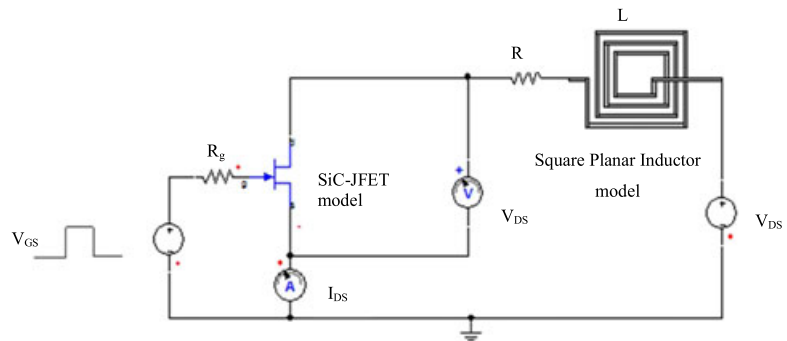
- The device under test, and the square, hexagonal, and octagonal planar inductors are printed directly on the PCB with different design parameters (see Table 5). The PCB substrate is made up of FR4 material with the dielectric constant,  $\epsilon_r$ , and the thicknesses are 4.4 and 1.6 mm.
- A noninductive film resistor used as a resistor  $R$  load.
- The silicon carbide junction field effect transistor device from SiCED as a high-speed switch.
- A driver to control the turn-on and the turn-off switching of the junction field effect transistor.
- A DC voltage source.
- A polypropylene capacitance used to stabilize the DC voltage source. More other details for the experimental platform are given in previous works.<sup>3,18</sup>

The proposed planar inductor model—detailed in Tables 1–4—is implemented in VHDL-AMS language and simulated in Simplorer platform.

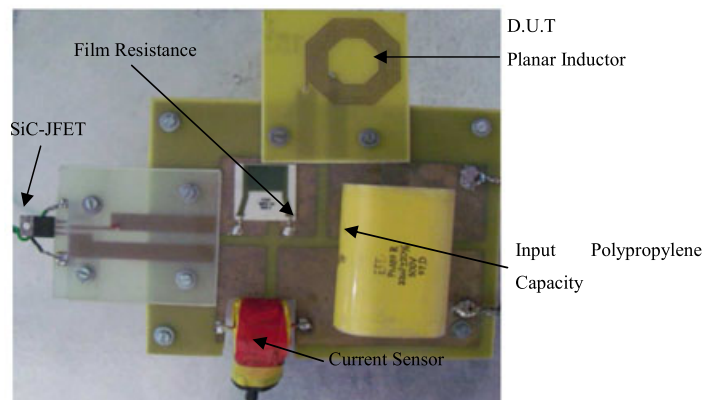
Figures 7–9 depict a comparative study between experimental data and simulation waveforms of the current and voltage waveforms for the square, hexagonal, and octagonal planar inductors. Table 7 gives the errors between experimental data and simulation results of the main switching parameters. These parameters are the current slope,  $di/dt$ , and the voltage slope,  $dv/dt$ , reverse recovery directly related to the spiral inductance.

### 3.4 | Validation and discussion

The authors specify here a validation process, which is defined by high accuracy and ease of use. Moreover, the frequency domain parameters refinement routine is not expensive from CPU cost time viewpoint as it only needs few loops. However,



(A)



(B)

**FIGURE 6**  $RL$  switching-cell circuit: A, electrical circuit; B, representation. D.U.T. indicates device under test; SiC JFET, silicon carbide junction field effect transistor

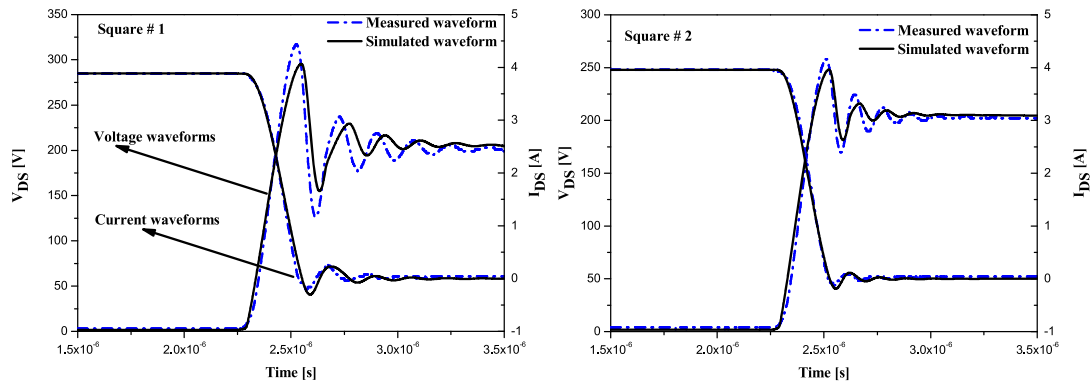


**FIGURE 7** Comparison of experimental and simulation results during turn-off transient of square planar inductors

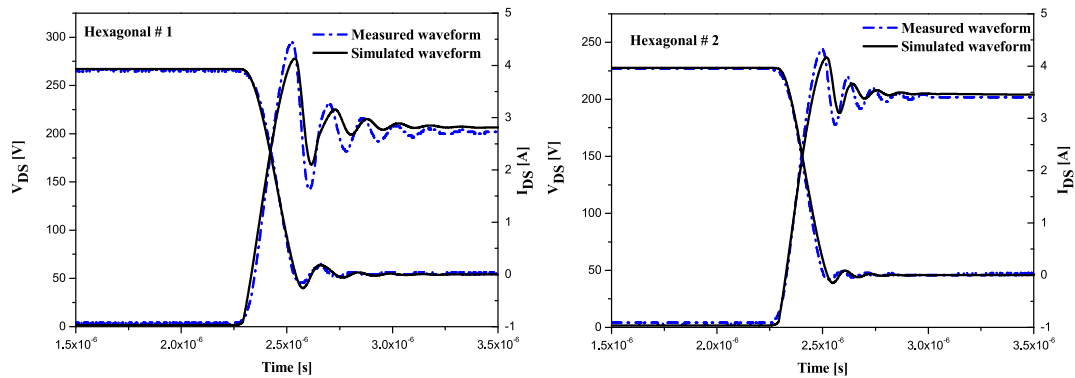


**FIGURE 8** Comparison of experimental and simulation results during turn-off transient of hexagonal planar inductors

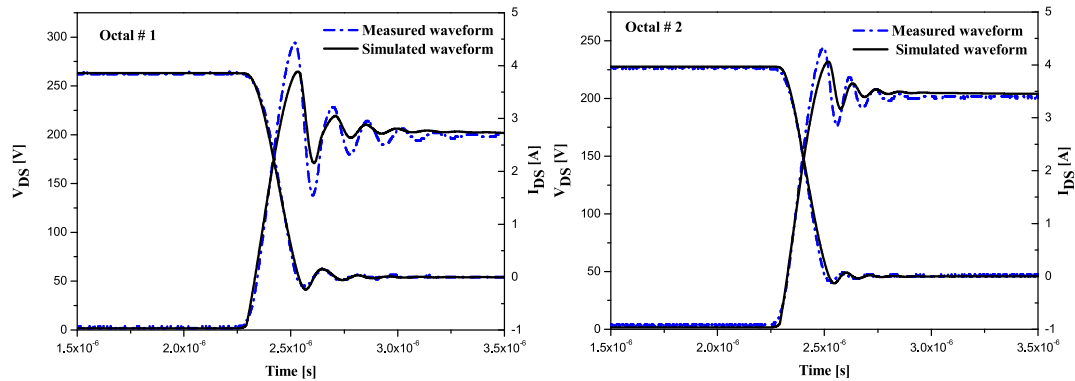


**FIGURE 9** Comparison of experimental and simulation results during turn-off transient of octagonal planar inductors

the success of this step is related to the accuracy of estimation model parameters. One source of error is due to the parasitic effect probes connections. However, it is the authors' opinion that such results do not reveal the validity of the model parameters during a simultaneous display of frequency and time domains.

Validity domain information should be favored. A validity domain is considered here to compute the progress of the error between experimental and simulated data of numerous spiral inductors (Table 6 and 7). At device level, a device engineer should appreciate the validity field of a physically based model. Table 6 summarizes the error between experimental and simulation. The error is less than 5% for the  $L_s$  and about 10% for the  $Z_{re}$  parameter. The  $L_s$  and  $Z_{re}$  represent the real and imaginary parts of the complex impedance of the planar inductor, respectively.

**TABLE 7** Switching parameter errors between simulation and experiment of different planar inductors during time domain validation

Inductor/Parameter		$di_R/dt$ (As – 1)	$dv_R/dt$ (As – 1)
Square 1	Simulation	$-1.98 \times 10^7$	$1.39 \times 10^9$
	Experimental	$-2.12 \times 10^7$	$1.52 \times 10^9$
	Error %	6.6	8.5
Hexagonal 1	Simulation	$-2.03 \times 10^7$	$1.34 \times 10^9$
	Experimental	$-2.17 \times 10^7$	$1.45 \times 10^9$
	Error %	6.4	7.5
Octagonal 1	Simulation	$-2.02 \times 10^7$	$1.37 \times 10^9$
	Experimental	$-2.02 \times 10^7$	$1.48 \times 10^9$
	Error %	5.1	7.4
Square 2	Simulation	$-2.09 \times 10^7$	$1.29 \times 10^9$
	Experimental	$-2.25 \times 10^7$	$1.4 \times 10^9$
	Error %	7	7.8
Hexagonal 2	Simulation	$-2.14 \times 10^7$	$1.29 \times 10^9$
	Experimental	$-2.29 \times 10^7$	$1.39 \times 10^9$
	Error %	6.5	7.1
Octagonal 2	Simulation	$-2.17 \times 10^7$	$1.27 \times 10^9$
	Experimental	$-2.32 \times 10^7$	$1.36 \times 10^9$
	Error %	6.4	6.6
Square 3	Simulation	$-2.15 \times 10^7$	$1.27 \times 10^9$
	Experimental	$-2.30 \times 10^7$	$1.38 \times 10^9$
	Error %	6.5	7.9
Hexagonal 3	Simulation	$-2.20 \times 10^7$	$1.24 \times 10^9$
	Experimental	$-2.31 \times 10^7$	$1.34 \times 10^9$
	Error %	4.7	7.4
Octagonal 3	Simulation	$-2.26 \times 10^7$	$1.30 \times 10^9$
	Experimental	$-2.34 \times 10^7$	$1.39 \times 10^9$
	Error %	3.4	6.4

Table 7 demonstrates that the error is less than 9% for the all switching parameters for different planar inductors; ie, the error is less than 7% for the  $di/dt$  and around 9% for  $dv/dt$  parameter. Therefore, the square inductor presents an error of less than 7% for the  $di/dt$  and around 8.5% for  $dv/dt$  parameter. The error of the hexagonal inductance is around 6.5% for the  $di/dt$  and 7.5% for  $dv/dt$ . The octagonal planar inductor presents an error of less than 6.4% for  $di/dt$  and 7.4% for  $dv/dt$ . The  $di/dt = -V/L$  at beginning of reverse recovery is directly related to the total inductance parameters.

These results show that errors in the square inductors during time and frequency domains ( $L_s$ ) are larger than those in the hexagonal and octagonal inductors except for square 1. Many authors declare that these errors are due to the rectangular angles in a square shape.<sup>19</sup> A good alternative is the adaptation of the polygonal design to obtain better performances.<sup>20,21</sup>

To highlight the obtained simulation results, we compared the proposed model with the most important planar models from the literature.<sup>22,23</sup>

- Model 1.<sup>22</sup> It presents an analytical planar inductor model for medical application. An accurate algorithm has been developed to determine the simplified lumped element equivalent model parameters for spiral inductor and its physical dimensions.

Table 8 presents the error between the experimental and simulation results of the planar inductors model 1 in terms of inductance value. The error of this model is between 1% and 8% compared with 5% of our model. However, the authors have not studied the validity of the proposed model in terms of series resistance value and for spirals having different geometries and various sizes.

- Model 2.<sup>23</sup> The authors present the design and the modeling of PCB planar inductors for single-chip communication systems. A validation process is performed by a comparative study between analytical model and experimental results

**TABLE 8** Error between measured and analytical results<sup>22</sup>

	Measurement Inductance Value, nH	Analytical Inductance Value, nH	Error, %
Ind 1	529.04	516.41	2.45
Ind 2	762.13	753.73	1.11
Ind 3	257.04	238.41	7.81
Ind 4	413.50	405.08	2.08
Ind 5	137.88	132.11	4.37

**TABLE 9** Error between measured and analytical results<sup>23</sup>

	Measurement	Analytical	Error, %
Inductance value, nH	95	100	5.8
Resistance value, $\Omega$	2.8	2.4	14.3

(Table 9). The error of this model is about 6% compared with 7% of our model in terms of inductance value, and the series resistance error is around 14% compared with 10% of our model. This study confirmed that the projected model is more accurate in terms of series resistance and presents a comparable error in terms of inductance value.

Various results have been satisfactory so far. For a large range of applied voltage, the physically based model is then sufficient. As many physically based spiral models use the similar parameter set, it is simple to extrapolate that these models will offer the same validity domain. The paper demonstrates that a physically based spiral inductor model may be used for precise simulation, as long as the design parameter is sufficient.

## 4 | CONCLUSION

In this paper, a spiral planar inductor physically based model is presented. The frequency and the time domain characteristics of each device in the model have been investigated extensively. The capacitances between adjacent turns, the substrate capacitance, the self and mutual inductances, the skin, and the proximity effects are considered and analyzed. The excellent accuracy of the results across all classes of spirals with various layouts and process parameters demonstrated the flexibility of the proposed model. Future work should concern the implementation of the proposed time-frequency domain algorithm in the Simplorer simulator to obtain optimal spiral inductor geometries, allowing designers to predict and optimize the quality factor.

## REFERENCES

- Ouyang Z, Andersen MAE. Overview of planar magnetic technology-fundamental properties. *IEEE Trans Power Electron.* 2014;29(9):4888-4900.
- Zhang W, Yipeng S, Mingkai M, Gilham DJ, Li Q, Lee FC. High-density integration of high-frequency high-current point-of-load (POL) modules with planar inductors. *Power Electron.* 2015;30:3.
- Ammouri A, Ben Salah W, Khachroumi S, Ben Salah T, Kourda F, Morel H. Development of a physically-based planar inductors VHDL-AMS model for integrated power converter design. *Eur Phys J Appl Phys.* 2014;66:20901.
- Chen M, Araghchini M, Afridi KK, Lang JH, Sullivan CR, Perreault DJ. A systematic approach to modeling impedances and current distribution in planar magnetics. *IEEE Trans Power Electron.* 2016;31:1.
- Han B, Song Y, Wang Z, Li J, Shi X. Verification of transmission line de-embedding method for on-chip spiral inductor based on electromagnetic simulation. *Int J Numer Modell: Electron Networks, Devices Fields*, Wiley 2015.
- Wang J, Liu J, Sun L, Zhou M. A novel method of analytically extracting model parameters for stacked transformers. *Int J Numer Modell: Electron Networks, Devices Fields.* 2016;29(2):255-264.
- Huo X, Chan PCH, Chen KJ, Luong HC. A physical model for on-chip spiral inductors with accurate substrate modeling. *IEEE Trans Electron Devices.* 2006;53(12):2942-2949.
- Han B, Wang D, Wang F, Wang S. Poles-zeros analysis and broadband equivalent circuit for on-chip spiral inductors. *Int J Numer Modell: Electron Networks, Devices Fields*, Wiley 2015:446-457.

9. Grover F. *Inductance Calculations: Working Formulas and Tables*. New York: Van Nostrand; 1946.
10. Greenhouse HM. Design of planar rectangular microelectronic inductors. *IEEE Trans Parts Hybrids Packag*. 1974;10(2):101-109.
11. Jenei S, Nauwelaers BKJC, Decoutere S. Physics-based closed-form inductance expression for compact modeling of integrated spiral inductors. *IEEE JSolid-State Circuits*. 2002;37(1):77-80.
12. Maheshwari V, Lavana S, Sengupta D, Kar R, Mandal D, Bhattacharjee AK. An explicit crosstalk aware delay modelling for on-chip VLSI RLC interconnect with skin effect. *Journal of Electron Devices*. 2011;10:499-505.
13. Jow U-M, Ghovanloo M. Design and optimization of printed spiral coils for efficient transcutaneous inductive power transmission. *IEEE Trans Biomed Circuits Syst*. 2007;1(3):193-202.
14. Hani F, Boulzazen H, Kadi M. Wideband characterization and modeling of coupled inductors under temperature variations. 2015 IEEE International Symposium on Electromagnetic Compatibility (EMC), 2015.
15. Yipeng S, Liu X, Lee CK, Ron Hui SY. On the relationship of quality factor and hollow winding structure of coreless printed spiral winding (CPSW) inductor. *IEEE Trans Power Electron*. 2012;27(6):3050-3056.
16. Stalf S. Printed inductors in RF consumer applications. *IEEE Trans Consum Electron*. 2001;47(3):426-435.
17. Kumada A, Okabe S, Hidaka K. Influences of probe geometry and experimental errors on spatial resolution of surface charge measurement with electrostatic probe. *IEEE Trans Dielectr Electr Insul*. 2005;12(6):1172-1181.
18. Mtimet S, Salah WB, Salah TB, Kourda F, Morel H. An advanced VHDL-AMS PiN diode model: towards simulation based design of power converters. *Int J Numer Modell: Electron Networks, Devices Fields*. 2014;28(3):287-300.
19. Mohan SS, Hershenson MM, Boyd SP, Lee TH. Simple accurate expressions for planar spiral inductors. *IEEE Journal of Solid-state Circuits*. 1999;34:10.
20. Ammouri A, Ben Salah T, Kourda F. Experimental analysis of planar spiral inductors. 2014 International Conference on Electrical Sciences and Technologies in Maghreb (CISTEM), 2014.
21. Stojanovic G, Zivanov L. Comparison of optimal design of different spiral inductors. 2004 24th International Conference on Microelectronics (IEEE Cat. No.04TH8716), 2004.
22. Eroglu A. Planar inductor design for high power applications. *Progress In Electromagnetics Research B*. 2011;35:53-67.
23. Chung J, Hamed-Hagh S. Design of PCB impedance matching inductors and antennas for single-chip communication systems. *International Journal of Microwave Science and Technology*. 2008;2008:7.

**How to cite this article:** Ammouri A, Ben Salah T, Morel H. A spiral planar inductor: An experimentally verified physically based model for frequency and time domains. *Int J Numer Model*. 2018;31:e2272. <https://doi.org/10.1002/jnm.2272>